Extended Material Point Method for the 3D Crack Problems†

Yong Liang⋆ | Xiong Zhang* | Yan Liu

[1]School of Aerospace Engineering, Tsinghua University, Beijing 100084, P R China

Correspondence
*Xiong Zhang, School of Aerospace Engineering, Tsinghua University, Beijing 100084, PR China.
Email: xzhang@tsinghua.edu.cn

Summary

The material point method (MPM) has demonstrated itself as an effective numerical method to simulate extreme events with large deformations including fracture problems. However, the traditional MPM encounters difficulties in simulating discontinuities due to its continuous nodal shape function. In this paper, The eXtended Material Point Method (XMPM) is proposed to simulate the 3D crack propagation. The XMPM modifies the particle displacement approximation by introducing the local enrichment functions based on the partition of unity into the MPM framework. To accurately trace the evolution of the crack surface, the XMPM employs both the level set method and an extra set of crack surface mesh, which is independent of the background grid. Only locally enriching the nodes near the crack makes the XMPM efficient and able to multiple cracks without extra tricks. Besides, a series of adaptive crack front processing methods, including crack front splitting, merging and locking with its meeting the material boundary, are developed in the XMPM framework to ensure the continuity and smoothness of the crack surface. Numerical examples demonstrate the capability of XMPM to simulate the discontinuity, calculate the fracture parameters and handle the evolution of the crack surface growth in 3D dynamic crack propagation.

KEYWORDS:
eXtended Material Point Method, 3D crack propagation, Fracture parameters

1 | INTRODUCTION

Fracture is a common failure mode in many engineering fields, which has resulted in major safety accidents and brings serious loss of life and property damage. With the rise of modern industry, the application of metal materials in engineering has increased rapidly, and with the continuous emergence of large-scale building structures, catastrophic accidents caused by fracture have increased dramatically, such as aircraft crash, bridge collapse, pressure vessel explosion[1], etc. Therefore, the study of fracture mechanics has important theoretical significance and engineering application prospect, which attracts researchers' attention.

Fracture mechanics, as a branch of solid mechanics, mainly focuses on the strength and propagation of cracked bodies. In the 1920s, Griffith[2] made a pioneering research for fracture mechanics and proposed a crack instability criterion based on the energy balance. Irwin[3] introduced the concept of stress intensity factor, established the crack growth criterion, and connected the energy release rate of Griffith theory with stress intensity factor, which laid a foundation for linearly elastic fracture mechanics. Paris[4] et al. then used stress intensity factor to analyze fatigue crack growth. Rice[5] and Cherepanov[6] proposed the concept of J-integral for elastic-plastic fracture to characterize the stress field strength at the crack tip, which is equivalent to energy release

†Supported by the National Natural Science Foundation of China (11672154) and Science Challenge Project (TZ2018002).
⋆Currently a postdoc in Department of Civil and Environmental Engineering, University of California, Berkeley, CA, 94720, United States

This article has been accepted for publication and undergone full peer review but has not been through the copyediting, typesetting, pagination and proofreading process which may lead to differences between this version and the Version of Record. Please cite this article as doi: 10.1002/nme.6653

rate in the case of linear elasticity and small-scale yield. J-integral and HRR singular field developed by Hutchinson, Rice and Rosengren[7] establish the theoretical framework of elastic-plastic fracture mechanics. The crack opening displacement criterion has also been widely used in the prediction of crack growth in elastic-plastic fracture. At present, fracture mechanics is still one of the most active fields in the study of solid mechanics. Experiments are the most direct means to study fracture problems, which provides a reliable basis for theoretical verification and numerical algorithm. However, most of the cracks are three-dimensional, the crack surface is complex and the propagation path is arbitrary. Due to the huge complexity, not only the theoretical analysis is difficult to progress, even many experimental methods face lots of difficulties. With the rapid development and improvement of computer technology and various numerical algorithms, numerical simulation has gradually become an effective means to study fracture problems due to its low cost, strong applicability and infinite repeatability.

The finite element method (FEM) has been widely used in fracture mechanics problems such as the conventional FEM with adaptive mesh[8], cohesive zone model[9], node force release method, and embedded discontinuous method[10]. The conventional FEM approximates the displacement field with continuous shape function, which requires the continuity of material in elements. Therefore, when dealing with the discontinuity such as crack growth and inclusion, the discontinuity has to be coincident with the element boundary, which greatly limits the arbitrary crack growth in space. To ensure that coincidence, a set of adaptive grid schemes is usually needed[8], which brings the computational burden, and the repeated mapping of physical quantities between the new and old grids will also influence calculation accuracy. Besides, the traditional Lagrangian FEM also encounters mesh distortion in the case of large deformation, which leads to great errors.

To overcome the difficulties of traditional FEM in simulating cracks, the extended finite element method (XFEM) is first proposed by Belytschko[11], which separates the description of crack from the grid description. Then, Moës[12] et al. introduced the Heaviside function and the crack tip asymptotic displacement field functions of a linear elastic case to represent crack surface and crack tip respectively. The XFEM introduces the discontinuous enrichment into original displacement approximation to represent the discontinuity based on the principle of the partition of unity[13,14], which allows the crack to pass through the elements so that remeshing is unnecessary while crack propagates. Besides, the XFEM uses the known solution to construct the enriched function base, so it can get more accurate results on the coarser mesh for the singular field while the traditional FEM has to refine the mesh. The theory of XFEM has been continuously developed after it is put forward. Generally, the Heaviside function is used as the enriched function for the crack surface. Many other enrichments such as bimaterial interface crack[15], orthotropic material crack[16], electromagnetic material crack[17], V-notch crack[18] and cohesive crack[19,20] are also proposed for the different cases. In addition, Belytschko[21], Daux[22], Budyn[23] and Taleghani[24] et al. proposed the corresponding enriched functions for crack bifurcation and multiple cracks intersection respectively. The XFEM has been widely used in many fields such as aerospace, civil engineering and mechanical engineering, which makes it one of the important methods to deal with the discontinuities, localization and fracture problems. However, the XFEM, which is based on the theory of standard FEM, still faces the numerical difficulty of mesh distortion when solving the problem with extreme large deformation.

In recent decades, the meshless method[25,26] has attracted more and more attention due to the difficulty of mesh distortion in grid-based methods while modelling large deformation problems. The meshless method abandons the grid and uses a group of particles to discretize the material domain, which reduces the grid dependence of traditional grid-based methods. There are about 30 kinds of meshless methods[27] depending on the weighted residual method and trial functions used. Many meshless methods have been applied to solve fracture problems. Belytschko[25,28,29,30] et al. used local refinement in EFG to improve the calculation accuracy of stress intensity factors and simulate both static and dynamic crack growth. Fleming[31] et al. proposed two kinds of crack tip enriched functions, which effectively reduced the numerical oscillation and improved the calculation accuracy of stress intensity factor. Rao[32,33] et al. applied EFG in heterogeneous fracture and nonlinear fracture. Liu[34] et al. used RKPM (Reproducing Kernel Particle Method) to simulate dynamic fracture. The meshless method is also applied to fracture problems by coupling with other numerical methods[35,36].

The material point method (MPM) is an extension of the FLIP (Fluid Implicit Method) method from fluid mechanics to solid mechanics by Sulsky et al.[37,38]. The MPM discretizes the material domain into a set of particles moving through the predefined Eulerian background grid, which is used as a computational scratch pad to solve the momentum equations. The solutions are then mapped back to update physical quantities at particles. The deformed grid is discarded and reset at the end of each time step, which makes the MPM avoids the mesh distortion for problems with large deformation. The MPM has been widely developed after it is put forward in many aspects especially in eliminating the "cell crossing noise", which seriously affects the computational accuracy. Bardenhagen[39] et al. first analyzed the causes in 2004 and proposed the generalized interpolation material point method (GIMP) based on the Petrov-Galerkin method to reduce the noise. The GIMP uses the shape function with C^1 continuity, which has the continuous gradient at the boundary of elements. The numerical examples show the GIMP

effectively suppresses the numerical noise and the stress oscillation. Many forms derived from the GIMP are also proposed such as cpGIMP[40] (continuous particle GIMP), uGIMP[41] (uniform GIMP) and also the iGIMP[42] (implicit GIMP). The original MPM can also be regarded as a special GIMP which takes the characteristic function as Dirac function. Later, a series of methods including the CPDI[43] (convected particle domain interpolation), DDMP[44] (dual domain material point), BSMPM[45] (B-spline MPM), IMPM[46] (improved MPM) and SGMP[47] (staggered grid MPM) have been proposed to eliminating the numerical noise, which makes the MPM itself greatly improved. Throughout the past several decades, the MPM has been continuously developed and applied successfully to many challenging problems such as hyper velocity impact[48,49], explosion[50,51,52], penetration[53,54], fragmentation[55,56], multiphase flow[57], fluid-structure interaction[58,59,60], etc.

Another potential application of MPM is dynamic fracture modelling due to the advantages in problems with extreme deformation. The original MPM uses a single grid with the continuous shape function, which prevents itself from modelling discontinuities. Nairn[61] proposed the CRAMP (MPM with CRAcks) to simulate the explicit cracks. The CRAMP employs multiple velocity fields and a line crossing algorithm is used to determine the velocity types. Nairn used the CRAMP to calculate the crack stress intensity factors[62] and model the propagation[63,64]. Liang[65] et al. modified the particle displacement approximation by introducing the discontinuous enriched function to represent the crack and simulated the crack propagation with J-integral and stress intensity factors. In addition, Kakouris[66,67] et al. introduced phase field in the MPM framework to model fracture behaviours. Cheon[68] et al. proposed an adaptive refinement process for the MPM also coupled with a phase-field fracture model to simulate crack propagation in brittle materials. Introducing the plasticity and softening in the constitutive model can also simulate the separation to some extent. Soga[69] et al. used Mohr-Coulomb, Cam-Clay and other derivatives to simulate the shear bands in the landslide cases. Shen[56] et al. used a Drucker-Prager model, a rate-dependent damage model and a bifurcation-based decohesion model to describe the behaviour of compression, tensile and localization respectively, and simulated the glass fragmentation under impact.

In this paper, the eXtended Material Point Method (XMPM) is proposed to model 3D crack problems. The XMPM modified the particle displacement approximation with local enrichment functions in the MPM framework just as what XFEM has done in FEM. The jump function is employed to represent the discontinuity on both sides of the crack. To accurately track the movement and evolution of the crack surface, both Level Set Method (LSM) and an extra set of mesh of the crack surface (crack surface mesh) are used in the XMPM. The level set function values are initialized and updated based on the crack surface mesh, used to compute the enriched function and carried by the particles as other physical quantities. It should be noted that only locally enriching the nodes near the crack makes the XMPM efficient and can simulate multiple cracks without extra tricks. Besides, a series of adaptive crack front processing methods is developed to ensure the continuity and smoothness of the crack surface while propagating. Numerical studies show that the XMPM is capable of modelling cracks including multiple uncrossed cracks, computing fracture parameters (J integral and stress intensity factors for both static and dynamic conditions), and simulating 3D crack propagation.

The rest of this paper is organized as follows: First, the MPM scheme and the XFEM are briefly reviewed in Section 2. The detailed formulation of the proposed XMPM is presented in Section 3, which also describes the LSM and crack surface mesh, time integration and update of particle variables. Section 4 presents the algorithm for computing fracture parameters and introduces the dynamic crack propagation law. Several numerical tests are carried out in Section 5 to validate the proposed method. Finally, some concluding remarks are drawn in Section 6.

2 | MATERIAL POINT METHOD

2.1 | Governing equations

The MPM seeks week solution of partial differential equations in the material domain Ω, which is given in the updated Lagrangian formulation as follows:

$$\int_{\Omega} \rho \ddot{u}_i \delta u_i \mathrm{d}\Omega + \int_{\Omega} \sigma_{ij} \delta u_{i,j} \mathrm{d}\Omega - \int_{\Omega} \rho b_i \delta u_i \mathrm{d}\Omega = 0 \tag{1}$$

where Γ_t is the prescribed traction boundary of Ω, ρ is the current density, the subscripts i and j indicate the components of the spatial variables following the Einstein convention, u_i is the displacement, σ_{ij} is the Cauchy stress and b_i is the body force per unit mass, respectively. The traction term is omitted for simplicity.

2.2 | MPM solution scheme

The MPM discretizes the material domain into a cluster of particles, which are also taken as the quadrature points. Then the discretized form of Eq.(1) can be written as

$$\sum_{p=1}^{n_p} m_p \ddot{u}_{ip} \delta u_{ip} + \sum_{p=1}^{n_p} V_p \sigma_{ijp} \delta u_{ip,j} - \sum_{p=1}^{n_p} m_p b_{ip} \delta u_{ip} = 0 \tag{2}$$

where n_p is the total number of the particles, m_p, V_p, u_{ip}, δu_{ip} and b_{ip} are the mass, volume, displacement, virtual displacement and body force of the particle p, respectively.

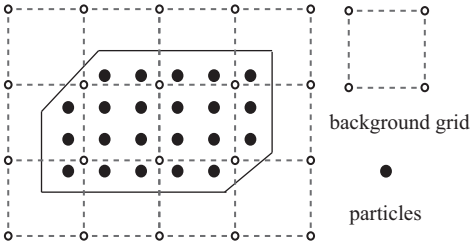

FIGURE 1 Typical MPM discretization

In the MPM, the particles are attached to the background grid at every time step. Therefore, the particle displacement u_{ip} can be obtained by interpolating the grid nodal displacement u_{iI} as

$$u_{ip} = \sum_I N_{Ip} u_{iI} \tag{3}$$

where the subscript p denotes the variables associated with the particle p, the subscript I denotes the variables associated with the grid node I, and N_{Ip} is the shape function of node I evaluated at the position of particle p. Similarly, other quantities of a particle such as velocity and acceleration can also be interpolated by the corresponding grid nodal quantities.

Substituting the quantities of particles including Eq.(3) into the discretized weak form Eq.(2) and invoking the arbitrariness of the virtual displacement δu_{iI} lead to the grid nodal momentum equation

$$\dot{p}_{iI} = f_{iI}^{\text{int}} + f_{iI}^{\text{ext}}, \quad \forall \boldsymbol{x}_I \notin \Gamma_u \tag{4}$$

where Γ_u denotes the displacement boundary of the material domain,

$$p_{iI} = m_I \dot{u}_{iI} \tag{5}$$

is the grid nodal momentum,

$$m_I = \sum_{p=1}^{n_p} N_{Ip} m_p \tag{6}$$

is the lumped grid nodal mass by row summation to improve the computational efficiency,

$$f_{iI}^{\text{int}} = -\sum_{p=1}^{n_p} V_p N_{Ip,j} \sigma_{ijp} \tag{7}$$

is the internal nodal force,

$$f_{iI}^{\text{ext}} = \sum_{p=1}^{n_p} m_p N_{Ip} b_{ip} \tag{8}$$

is the external nodal force.

2.3 | Extended finite element method

The foundation of the XFEM is the partition of unity[70,71], which is a set of function given in domain Ω as

$$\sum_I \varphi_I(\boldsymbol{x}) = 1, \forall \boldsymbol{x} \in \Omega \tag{9}$$

The property of the partition of unity is that any function $\phi(\boldsymbol{x})$ can be reproduced by a product of the partition of unity functions with $\phi(\boldsymbol{x})$. In the XFEM, the standard displacement based finite element approximation is modified by introducing the enrichment of additional functions with the framework of partition of unity as

$$u_i^{\mathrm{h}}(\boldsymbol{x}) = \sum_I N_I(\boldsymbol{x})\, u_{iI} + \sum_I \varphi_I(\boldsymbol{x})\, \phi(\boldsymbol{x})\, q_{iI} \tag{10}$$

where N_I is the standard FEM shape function, u_{iI} is the standard nodal degree of freedom, and the subscript I is associated to node I. The first term of the right hand in Eq.(10) is the standard FEM approximation, while the second term is the enrichment part. The unknown nodal value q_{iI} is to adjust the enrichment to be the best approximations of the solution. It should be noted that the shape functions N_I and φ_I, indicated in the above, need not be the same. However, the same functions are generally used, i.e. $\varphi_I(\boldsymbol{x}) = N_I(\boldsymbol{x})$.

The choice of the enrichment functions is determined by the specific applications. For the crack problems with strong discontinuities at both sides, the Heaviside functions is generally used, which is defined as

$$H(\psi(\boldsymbol{x})) = \begin{cases} 1 & \psi(\boldsymbol{x}) > 0 \\ -1 & \text{otherwise} \end{cases} \tag{11}$$

Therefore, the modified displacement in the XFEM is rewritten as

$$u_i^{\mathrm{h}}(\boldsymbol{x}) = \sum_I N_I(\boldsymbol{x})\, u_{iI} + \sum_I N_I(\boldsymbol{x})\, H(\psi(\boldsymbol{x}))\, q_{iI} \tag{12}$$

where $\psi(\boldsymbol{x})$ is the level set functions introduced in section 3.1.1.

3 | EXTENDED MATERIAL POINT METHOD

3.1 | Crack surface description

The XMPM describes the crack surface independently from the grid. For constructing the enriched function, calculating the fracture parameters and accomplishing the crack propagation, the XMPM combined the level set method and a set of crack surface mesh to describe and track the crack surface.

3.1.1 | Level set method

Level set method[72] is usually used for tracking moving interfaces or the discontinuities[73] by the zero level set of a function $\psi(\boldsymbol{x}(t), t) = 0$. This function is one dimension higher than that of the interface. In general, a crack surface Γ_{C} can be formulated by the zero level set functions as

$$\Gamma_{\mathrm{C}} = \{\boldsymbol{x} : \psi(\boldsymbol{x}, t) = 0\} \tag{13}$$

The initial level set function values is typically determined as

$$\psi(\boldsymbol{x}, 0) = \min \parallel \boldsymbol{x} - \hat{\boldsymbol{x}} \parallel \cdot \mathrm{sign}(\boldsymbol{n} \cdot (\boldsymbol{x} - \hat{\boldsymbol{x}})) \tag{14}$$

where ψ is the signed distance, $\hat{\boldsymbol{x}}$ is the nearest point to the position $\boldsymbol{x}$ on the crack plane, and $\boldsymbol{n}$ is the unit normal vector of the crack surface, the initial position of which is given by $\psi(\boldsymbol{x}, 0) = 0$. Then the motion can be determined by an evolution equation for $\psi(\boldsymbol{x}, t)$ by taking the time derivative of $\psi(\boldsymbol{x}, t) = 0$. In addition, if the crack doesn't penetrate the object completely, another level set function is needed to describe the crack tip (a spatial curve in 3D). As shown in Fig.2, the level set function ψ represents the signed normal distance from particle p to the crack line ($\psi = 0$) and φ represents the signed normal distance from particle $p$to the line perpendicular to the crack line ($\varphi = 0$).

Introducing the LSM into the XMPM makes it convenient to calculate the value of the enriched function. At the beginning of the simulation, the LSM values of particles are initialized according to the given crack surface. Since the background grid will be discarded after each time step, the LSM values, as other physical quantities, are carried by the particles and updated to track the crack surface. Besides, only the particles near the crack need to be initialized so that multiple uncrossed cracks can be handled directly by the XMPM. The LSM is sufficient to simulate the discontinuities. However, while calculating the fracture parameters and modelling the crack growth, it needs to reconstruct the crack front position, which will not only bring additional calculation, but also affect the computational accuracy . Therefore, an explicit description of the crack surface will be necessary.

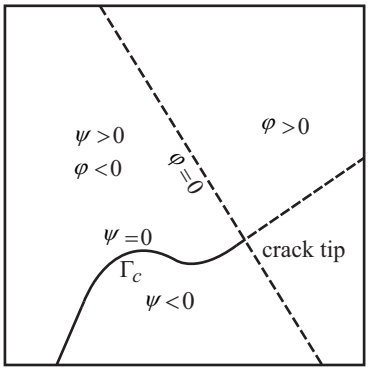

FIGURE 2 Level set surfaces defining the crack line and the tips

3.1.2 | Crack surface mesh

The explicit description refers to generating a set of mesh to representing the crack surface. A 3D crack surface is generally a spatial curved surface and the XMPM discretizes it into a set of triangular elements as shown in Fig.3. While simulating crack growth, the newly generated crack surface will also be discretized into triangular elements, which will be described in Section 4. The crack surface mesh will be used to construct the local coordinate system of the crack front and provide the crack tip opening displacement when calculating the fracture parameters of the crack tip. In addition, the crack surface mesh will also be used to initialize and update the LSM values. It is necessary to update the crack surface position after each time step in the same way as that of the material point.

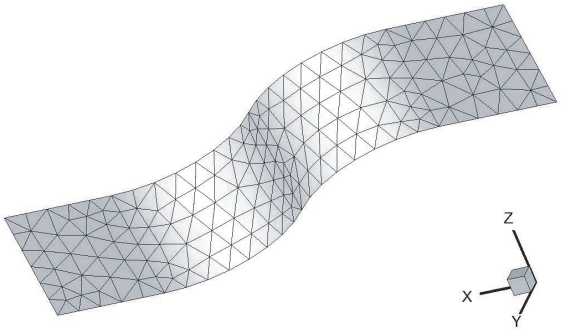

FIGURE 3 A 3D crack surface discretized into triangular elements

3.2 | XMPM solution scheme

3.2.1 | Displacement approximation

The XMPM introduces the discontinuous parts into the standard MPM displacement approximation to describe the discontinuity of the crack, which is given as

$$u_{ip} = u_{ip,\text{cont}} + u_{ip,\text{discont}} \tag{15}$$

The continuous part is the same as the standard MPM:

$$u_{ip,\text{cont}} = \sum_{I \in S}^{n_g} N_{Ip} u_{iI} \tag{16}$$

while the discontinuous part can be written as

$$u_{ip,\text{discont}} = \sum_{R\in S_C}^{n_c} H_p N_{Rp} q_{iR} \tag{17}$$

where S is the total set of grid nodes, n_g is the number of S, S_C is the set of nodes of the elements cut by the crack, n_c is the number of S_C, u_{iI} and q_{iR} are the the corresponding degrees of freedom for the standard and Heaviside enrichment, respectively. H_p represents the position of particle p relative to the crack, which is determined as

$$H_p = H(\psi(\boldsymbol{x}_p)) = \begin{cases} 1 & \psi(\boldsymbol{x}_p) > 0 \\ -1 & \text{otherwise} \end{cases} \tag{18}$$

3.2.2 | Enriched nodes

Based on the crack surface mesh, the elements cut by the crack can be determined. The nodes of those elements completely cut by a crack are enriched. Therefore, parts of nodes of the elements including the crack tip are also enriched, which causes the crack size in the simulation to be slightly larger than the actual size, but less than one element size.

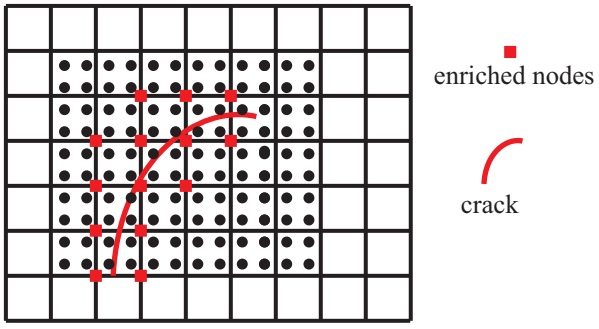

FIGURE 4 Enriched nodes of elements cut by the crack

3.2.3 | Grid nodal momentum equation

Similarly, substituting the displacement approximation Eq.(15) into the discretized weak form leads to the formulation of the proposed XMPM as

$$\begin{aligned}
&\sum_{p=1}^{n_p} m_p \left[\sum_{I\in S}^{n_g} N_{Ip}\delta u_{iI} + \sum_{R\in S_C}^{n_c} H_p N_{Rp}\delta q_{iR}\right]\left[\sum_{J\in S}^{n_g} N_{Jp}\ddot{u}_{iJ} + \sum_{L\in S_C}^{n_c} H_p N_{Lp}\ddot{q}_{iL}\right] + \\
&\sum_{p=1}^{n_p} \frac{m_p}{\rho_p}\sigma_{ijp}\left[\sum_{I\in S}^{n_g} N_{Ip,j}\delta u_{iI} + \sum_{R\in S_C}^{n_c} H_p N_{Rp,j}\delta q_{iR}\right] = \\
&\sum_{p=1}^{n_p} m_p b_{ip}\left[\sum_{I\in S}^{n_g} N_{Ip}\delta u_{iI} + \sum_{R\in S_C}^{n_c} H_p N_{Rp}\delta q_{iR}\right]
\end{aligned} \tag{19}$$

Invoking the arbitrariness of δu_{iI} and δq_{iR}, Eq.(19) can be rewritten in matrix form as

$$\begin{Bmatrix} [\dot{p}_{iI}] \\ [\dot{p}^*_{iR}] \end{Bmatrix} = \begin{bmatrix} [m_{IJ}] & [m^*_{IL}] \\ [m^*_{RJ}] & [m_{RL}] \end{bmatrix} \begin{Bmatrix} [\ddot{u}_{iJ}] \\ [\ddot{q}_{iL}] \end{Bmatrix} = \begin{Bmatrix} [f_{iI}] \\ [f^*_{iR}] \end{Bmatrix} \tag{20}$$

where

$$m_{IJ} = \sum_{p=1}^{n_p} m_p N_{Ip} N_{Jp} \qquad m^*_{IL} = \sum_{p=1}^{n_p} m_p N_{Ip} H_p N_{Lp} \tag{21}$$

$$m^*_{RJ} = \sum_{p=1}^{n_p} m_p H_p N_{Rp} N_{Jp} \qquad m_{RL} = \sum_{p=1}^{n_p} m_p N_{Rp} N_{Lp} \tag{22}$$

are the mass matrix and

$$f_{iI} = -\sum_{p=1}^{n_p} \frac{m_p}{\rho_p} N_{Ip,j} \sigma_{ijp} + \sum_{p=1}^{n_p} m_p N_{Ip} b_{ip} \tag{23}$$

$$f^*_{iR} = -\sum_{p=1}^{n_p} \frac{m_p}{\rho_p} H_p N_{Rp,j} \sigma_{ijp} + \sum_{p=1}^{n_p} m_p H_p N_{Rp} b_{ip} \tag{24}$$

are the nodal forces.

3.2.4 | Lumped mass matrix

The XMPM is proposed for fracture problems, whose duration is very small. So that an explicit method with a very small timestep is required to accurately capture the high-frequency response. A lumped mass matrix is usually used in an explicit method because of the low computational cost.

Observe the mass matrix in Eq.(20). It consists of four mass sub-matrices given in Eq.(21) and Eq.(22). The subscripts, I and J, correspond to all the nodes while R and L just represent the enriched nodes. Therefore, the mass sub-matrices $[m_{IJ}]$ and $[m_{RL}]$ are the square matrices of dimensions n_g and n_c respectively while the coupled mass sub-matrices m^*_{IL} and m^*_{RJ} are not the square matrices. m^*_{IL} is the matrix of dimension $n_g * n_c$ and m^*_{RJ} is the matrix of dimension $n_c * n_g$. As introduced in section 3.2.2, only the nodes of the elements cut by the crack are enriched, so we usually have $n_c \ll n_g$. The nodal mass matrix can't be lumped by row summation as the conventional MPM. To expand the mass matrix to a square matrix, the set of nodes $S - S_C$ are also enriched virtually. Then the mass sub-matrices can be lumped as

$$m_I = \sum_{J\in S}^{n_g} m_{IJ} = \sum_{J\in S}^{n_g} \sum_{p=1}^{n_p} m_p N_{Ip} N_{Jp} = \sum_{p=1}^{n_p} m_p N_{Ip} \tag{25}$$

$$m_R = \sum_{L\in S}^{n_g} m_{RL} = \sum_{L\in S}^{n_g} \sum_{p=1}^{n_p} m_p N_{Rp} N_{Lp} = \sum_{p=1}^{n_p} m_p N_{Rp} \tag{26}$$

$$m^*_I = \sum_{L\in S}^{n_g} m^*_{IL} = \sum_{L\in S}^{n_g} \sum_{p=1}^{n_p} m_p H_p N_{Ip} N_{Lp} = \sum_{p=1}^{n_p} m_p H_p N_{Ip} \tag{27}$$

$$m^*_R = \sum_{J\in S}^{n_g} m^*_{RJ} = \sum_{J\in S}^{n_g} \sum_{p=1}^{n_p} m_p H_p N_{Rp} N_{Jp} = \sum_{p=1}^{n_p} m_p H_p N_{Rp} \tag{28}$$

The momentum equation of grid node I is given as

$$\begin{Bmatrix} \dot{p}_{iI} \\ \dot{p}^*_{iI} \end{Bmatrix} = \begin{bmatrix} m_I & m^*_I \\ m^*_I & m_I \end{bmatrix} \begin{Bmatrix} \ddot{u}_{iI} \\ \ddot{q}_{iI} \end{Bmatrix} = \begin{Bmatrix} f_{iI} \\ f^*_{iI} \end{Bmatrix} \tag{29}$$

However, for the virtually enriched nodes, the mass matrix is not full rank. Taking a virtually enriched node R as shown in Fig.5 for example, it doesn't belong to the elements cut by the crack and is away from the crack so that we have $H_p \equiv H_R$. According to Eq.(25) to Eq.(28),

$$m_R = H_R m^*_R \tag{30}$$

Then the determinant of the mass matrix of node R is

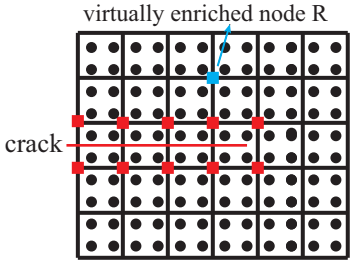

FIGURE 5 Virtually enriched nodes

$$\det\left(M_R\right) = m_R \cdot m_R - m_R^* \cdot m_R^* = 0 \tag{31}$$

which means that there is only one independent equation for the virtually enriched node R

$$m_R \ddot{u}_{iR} + m_R^* \ddot{q}_{iR} = f_{iR} \tag{32}$$

Considering the contribution of the grid node R while updating the particle information, taking the velocity for example, the increment is given as

$$\Delta v_{ip}^R = \Delta t \left(N_{Rp}\ddot{u}_{iR} + H_p N_{Rp}\ddot{q}_{iR}\right) = \Delta t N_{Rp}\left(\ddot{u}_{iR} + H_R\ddot{q}_{iR}\right) \tag{33}$$

The combined term $\ddot{u}_{iR} + H_R\ddot{q}_{iR}$ is needed to update the particle velocity, which can be solved by the Eq.(32) as

$$\ddot{u}_{iR} + H_R\ddot{q}_{iR} = \frac{f_{iR}}{m_R} \tag{34}$$

The form is the same as that of the conventional MPM. In conclusion, the virtually enriched nodes degenerate to the conventional grid node. The XMPM treat them as the conventional MPM. However, for the indeed enriched nodes, the momentum equation given in Eq.(29) need to be solved.

3.2.5 | Update of the particle information

As the conventional MPM, the XMPM stores all material properties on the particles. After solving the grid nodal momentum equations, the grid nodal velocities and accelerations are mapped back to the corresponding particles to update their positions and velocities. The central difference method[38] is taken as the time integration scheme in the XMPM. Therefore, the particle position and velocity can be obtained as follows,

$$x_{ip}^{n+1} = x_{ip}^n + \Delta t^{n+1/2}\left(\sum_{I\in S}^{n_g} N_{Ip}^n \dot{u}_{iI}^{n+1/2} + \sum_{R\in S_C}^{n_c} H_p N_{Rp}^n \dot{q}_{iR}^{n+1/2}\right) \tag{35}$$

$$v_{ip}^{n+1/2} = v_{ip}^{n-1/2} + \Delta t^n\left(\sum_{I\in S}^{n_g} N_{Ip}^n \ddot{u}_{iI}^n + \sum_{R\in S_C}^{n_c} H_p N_{Rp}^n \ddot{q}_{iR}^n\right) \tag{36}$$

where the superscript n, $n \pm 1/2$ and $n \pm 1$ represent the time step as shown in Fig.6.

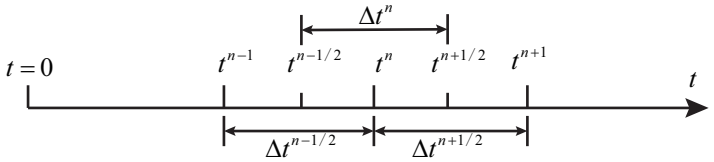

FIGURE 6 Leapfrog time integrator scheme

The enriched nodes only exist locally around the crack. Due to the compactness of the shape function, the Eq.(35) and Eq.(36) degenerate to the form as

$$x_{ip}^{n+1} = x_{ip}^n + \Delta t^{n+1/2}\sum_{I\in S}^{n_g} N_{Ip}^n \dot{u}_{iI}^{n+1/2} \tag{37}$$

$$v_{ip}^{n+1/2} = v_{ip}^{n-1/2} + \Delta t^n \sum_{I\in S}^{n_g} N_{Ip}^n \ddot{u}_{iI}^n \tag{38}$$

for the particles located in the cells which doesn't contain any enriched nodes. Eq.(37) and (38) are the formulations to update the particle information used in the conventional MPM with central difference method. That's to say, the XMPM can degenerate to the conventional MPM when there is no crack or in the area away from the crack. Hence the XMPM costs only a little extra computation effort compared to the original MPM.

To update the particle information, we need to solve Eq.(29) for each enriched node and Eq.(32) for each unenriched node. However, only the combined term $\ddot{u}_{iI} + H_p\ddot{q}_{iI}$ is needed for the enriched node so that there is no need to solve the Eq.(29) directly. Take the update of velocity for example, the Eq.(36) can be rewritten as

$$v_{ip}^{n+1/2} = v_{ip}^{n-1/2} + \Delta t^n \left(\sum_{I\in S, I\notin S_C}^{n_g-n_c} N_{Ip}^n \ddot{u}_{iI}^n + \sum_{I\in S_C}^{n_c} N_{Ip}^n \left(\ddot{u}_{iI}^n + H_p \ddot{q}_{iI}^n \right) \right) \tag{39}$$

Besides, multiplying the second equation in Eq.(29) by H_p and then adding it to the first equation result in

$$\dot{p}_{iI} + H_p \dot{p}_{iI}^* = \left(m_I + H_p m_I^* \right) \ddot{u}_{iI} + \left(m_I^* + H_p m_I \right) \ddot{q}_{iI} \tag{40}$$

Invoking $H_p H_p = 1$, we have

$$\dot{p}_{iI} + H_p \dot{p}_{iI}^* = \left(m_I + H_p m_I^* \right) \ddot{u}_{iI} + \left(H_p m_I^* + m_I \right) H_p \ddot{q}_{iI} = \left(m_I + H_p m_I^* \right) \left(\ddot{u}_{iI} + H_p \ddot{q}_{iI} \right) \tag{41}$$

Then, the combined term $\ddot{u}_{iI} + H_p\ddot{q}_{iI}$ can be obtained as

$$\ddot{u}_{iI} + H_p \ddot{q}_{iI} = \frac{\dot{p}_{iI} + H_p \dot{p}_{iI}^*}{m_I + H_p m_I^*} \tag{42}$$

Substituting Eq.(42) into Eq.(39), the formulation for updating particle velocity in XMPM is finally given as

$$v_{ip}^{n+1/2} = v_{ip}^{n-1/2} + \Delta t^n \left(\sum_{I\in S, I\notin S_C}^{n_g-n_c} N_{Ip}^n \frac{\dot{p}_{iI}^n}{m_I} + \sum_{I\in S_C}^{n_c} N_{Ip}^n \left(\frac{\dot{p}_{iI}^n + H_p \dot{p}_{iI}^{*,n}}{m_I + H_p m_I^*} \right) \right) \tag{43}$$

Similarly, the formulation for updating particle position is given as

$$x_{ip}^{n+1} = x_{ip}^n + \Delta t^{n+1/2} \left(\sum_{I\in S, I\notin S_C}^{n_g-n_c} N_{Ip}^n \frac{p_{iI}^{n+1/2}}{m_I} + \sum_{I\in S_C}^{n_c} N_{Ip}^n \left(\frac{p_{iI}^{n+1/2} + H_p p_{iI}^{*,n+1/2}}{m_I + H_p m_I^*} \right) \right) \tag{44}$$

Besides, the XMPM updates the stress state at particles as the conventional MPM to inherit the Lagrangian properties and the rate form of the constitutive models is used for nonlinear analysis. So the strain rate $\dot{\varepsilon}_{ij}$ and vorticity Ω_{ij} at particle p are required. They can be obtained from the velocity gradient of the background grid cell as

$$\dot{\varepsilon}_{ijp} = \frac{1}{2} \left(\sum_{I\in S, I\notin S_C}^{n_g-n_c} \left(N_{Ip,j} \frac{p_{iI}}{m_I} + N_{Ip,i}^n \frac{p_{jI}}{m_I} \right) + \sum_{I\in S_C}^{n_c} \left(N_{Ip,j} \left(\frac{p_{iI} + H_p p_{iI}^*}{m_I + H_p m_I^*} \right) + N_{Ip,i} \left(\frac{p_{jI} + H_p p_{jI}^*}{m_I + H_p m_I^*} \right) \right) \right) \tag{45}$$

$$\Omega_{ijp} = \frac{1}{2} \left(\sum_{I\in S, I\notin S_C}^{n_g-n_c} \left(N_{Ip,j} \frac{p_{iI}}{m_I} - N_{Ip,i}^n \frac{p_{jI}}{m_I} \right) + \sum_{I\in S_C}^{n_c} \left(N_{Ip,j} \left(\frac{p_{iI} + H_p p_{iI}^*}{m_I + H_p m_I^*} \right) - N_{Ip,i} \left(\frac{p_{jI} + H_p p_{jI}^*}{m_I + H_p m_I^*} \right) \right) \right) \tag{46}$$

Furthermore, we can observe that all the formulations used in the XMPM are very similar to that in the conventional MPM. Therefore, the XMPM is easy to be implemented in a conventional MPM code, such as the MPM3D code[53]. The XMPM can also be realized with the option USL, USF or MUSL. The differences between the original MPM and the XMPM can be concluded as follows: 1) At the beginning of the simulation, initialize the LSM values of particles and generate the crack surface mesh; 2) In each time step, the position of the crack surface mesh needs to be updated; 3) More quantities need to be calculated referred to the enriched degrees of freedom. The MUSL scheme is used in all the following simulations.

4 | THE DYNAMIC FRACTURE PARAMETERS AND CRACK PROPAGATION

The XMPM enhances the ability of simulating cracks in the MPM framework. To further model the crack growth, the calculation of the fracture parameters such as J-integral and stress intensity factors is of great necessity.

4.1 | J-integral

J-integral is a key fracture parameter put forward by Cherepanov[6] and Rice[5] independently to characterize the stress and strain intensity at the crack tip. At first, the concept of J-integral was limited to the elastic static condition. Then, the concept of dynamic J-integral is proposed for the dynamic crack growth problem and the body force, inertial force are also considered. The dynamic J-integral used in this paper was proposed by Nishioka[74] et al. in 1983 given as

$$J_m = \lim_{\varepsilon\to 0}\int_{\Gamma_\varepsilon}\left[(W+E)\,n_m - \sigma_{ij}n_j\frac{\partial u_i}{\partial x_m}\right]\mathrm{dS} \tag{47}$$

$$= \lim_{\varepsilon\to 0}\left\{\int_{\Gamma+\Gamma_C}\left[(W+E)\,n_m - \sigma_{ij}n_j\frac{\partial u_i}{\partial x_m}\right]\mathrm{dS} + \int_{V_\Gamma - V_\varepsilon}\rho\left[\frac{\partial^2 u_i}{\partial t^2}\frac{\partial u_i}{\partial x_m} - \frac{\partial u_i}{\partial t}\frac{\partial^2 u_i}{\partial t\partial x_m}\right]\mathrm{dV}\right\} \tag{48}$$

where $W = \int \sigma_{ij}\mathrm{d}\varepsilon_{ij}$ is the stress work density, $E = \frac{1}{2}\rho\dot{u}_i\dot{u}_i$ is the kinetic energy density. As shown in Fig.7, n_m is the cosine of the external normal vector, Γ_ε is the arbitrary integration path near the crack tip, Γ is the arbitrary integration path far from the crack tip, Γ_C is the crack surface surrounded by Γ, V_Γ is the integral surface surrounded by the integration path $\Gamma+\Gamma_C$, and V_ε is the integral surface surrounded by the integral path Γ_ε. The dynamic J-integral defined by Nishioka has the physical meaning of dynamic energy release rate, is independent of the selected path, and can be partitioned into dynamic stress intensity factors. Physically, the region V_ε is considered as the process zone in which fracture occurs. For numerical simulations, only the far-field paths can be used to compute the integral. Therefore, the following expression[75] is considered for the dynamic J-integral.

$$J_m = \int_{\Gamma+\Gamma_C}\left[(W+E)\,n_m - \sigma_{ij}n_j\frac{\partial u_i}{\partial x_m}\right]\mathrm{dS} + \int_{V_\Gamma}\rho\left[\frac{\partial^2 u_i}{\partial t^2}\frac{\partial u_i}{\partial x_m} - \frac{\partial u_i}{\partial t}\frac{\partial^2 u_i}{\partial t\partial x_m}\right]\mathrm{dV} \tag{49}$$

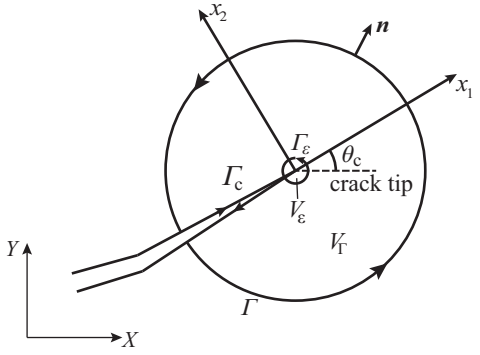

FIGURE 7 The J-integral path around the crack tip

It's convenient to construct an integral curve in 2D. However, in the 3D problem, the crack tip is no longer a point, but a spatial curve. As shown in Fig.8, the J-integral is performed on an $x1-x2$ plane in crack-tip local coordinates, which is perpendicular to the crack front and has the origin located at the crack front. A circular integral path is adopted in this paper and MLS is used to reconstruct the physical quantities of the integral points.

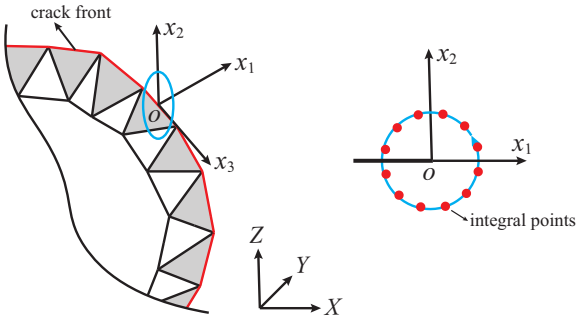

FIGURE 8 The J-integral path in 3D

4.2 | Stress intensity factor

With the dynamic J-integral, we have the energy release rate $G = J_1$. For the case of isotropic and linear elastic materials, the dynamic stress intensity factors can be further calculated. The relationship between the dynamic stress intensity factor and the energy release rate is given[74] as

$$G = \frac{1}{2\mu}\left\{A_{\mathrm{I}}(C)\,K_{\mathrm{I}}^2 + A_{\mathrm{II}}(C)\,K_{\mathrm{II}}^2 + A_{\mathrm{III}}(C)\,K_{\mathrm{III}}^2\right\} \tag{50}$$

where μ is the shear modulus, A_{I}, A_{II} and A_{III} are the function of the crack propagation velocity C defined as

$$A_{\mathrm{I}}(C) = \frac{\beta_1\left(1-\beta_2^2\right)}{D(C)},\ A_{\mathrm{II}}(C) = \frac{\beta_2\left(1-\beta_2^2\right)}{D(C)},\ A_{\mathrm{III}}(C) = \frac{1}{\beta_2} \tag{51}$$

where $D(C) = 4\beta_1\beta_2 - \left(1+\beta_2^2\right)^2$, β_1 and β_2 are defined by the crack propagation velocity C, dilatational-wave speed C_{d} and shear-wave speed C_{s} as

$$\beta_1^2 = 1 - \frac{C^2}{C_{\mathrm{d}}^2},\ \beta_2^2 = 1 - \frac{C^2}{C_{\mathrm{s}}^2} \tag{52}$$

Considering the relationship between dynamic stress intensity factors and crack opening displacement δ,

$$\frac{K_{\mathrm{II}}}{K_{\mathrm{I}}} = \frac{\delta_{\mathrm{II}}}{\delta_{\mathrm{I}}}\frac{\beta_1}{\beta_2},\ \frac{K_{\mathrm{III}}}{K_{\mathrm{I}}} = \frac{\delta_{\mathrm{III}}}{\delta_{\mathrm{I}}}\frac{\beta_1\beta_2\left(1-\beta_2^2\right)}{D(C)} \tag{53}$$

The explicit expression of dynamic stress intensity factor can be obtained[75] as

$$K_{\mathrm{M}} = \frac{\delta_{\mathrm{M}}}{A_{\mathrm{M}}(C)}\hat{K},\ (\mathrm{M} = \mathrm{I}, \mathrm{II}, \mathrm{III}) \tag{54}$$

where

$$\hat{K} = \left\{\frac{2\mu G}{\delta_{\mathrm{I}}^2/A_{\mathrm{I}} + \delta_{\mathrm{II}}^2/A_{\mathrm{II}} + \delta_{\mathrm{III}}^2/A_{\mathrm{III}}}\right\}^{1/2} \tag{55}$$

4.3 | Crack propagation

The classical strength failure criterion usually takes the stress as the parameter, while in fracture mechanics the stress intensity factor is usually used as the control parameter to establish the failure criterion, which can be expressed as

$$K = K_{\mathrm{C}} \tag{56}$$

where K_{C} is the critical value of the stress intensity factor and represents the fracture toughness of the material.

4.3.1 | Dynamic crack propagation law

"The maximum stress criterion" was first studied by Erdogan and Sih[76] in 1963 both experimentally and analytically and can be stated as "the crack will start to grow from the tip in the direction along which the tangential stress σ_θ, is maximum and the shear stress $\tau_{r\theta}$, is zero". By maximizing the hoop stress near the crack tip, the maximum hoop stress angle θ_{c} can be obtained as[77]

$$\theta_{\mathrm{c}} = 2\arctan\left[\frac{1}{4}\left(\frac{K_{\mathrm{I}}}{K_{\mathrm{II}}} - \mathrm{sign}(K_{\mathrm{II}})\left(8 + \left(\frac{K_{\mathrm{I}}}{K_{\mathrm{II}}}\right)^2\right)^{1/2}\right)\right] \tag{57}$$

Then the corresponding maximum hoop stress intensity K^* can be computed[78] by

$$K^* = \cos^3\left(\frac{\theta_{\mathrm{c}}}{2}\right)K_{\mathrm{I}} - \frac{3}{2}\cos\left(\frac{\theta_{\mathrm{c}}}{2}\right)\sin\left(\theta_{\mathrm{c}}\right)K_{\mathrm{II}} \tag{58}$$

where K^* is the dynamic maximum hoop stress intensity factor and K_{IC} is the dynamic crack initiation toughness of the material obtained from experiments. The crack propagates when K^* reaches K_{IC}.

The crack propagates when the dynamic maximum hoop stress intensity factor K^* reached the dynamic crack initiation toughness K_{IC}, which is a material property and can be obtained from experiments. The crack propagation velocity C can be

determined by making K^* equals to the dynamic crack growth toughness K_{ID} and the relationship between K_{IC} and K_{ID} is [78,79]

$$K_{\mathrm{ID}}(C) = \frac{K_{\mathrm{IC}}}{1 - \left(\frac{C}{C_{\mathrm{R}}}\right)} \tag{59}$$

where C_{R} is the Rayleigh-wave speed. Thus the crack propagation velocity C can be obtained from Eq.(59) as

$$C = \begin{cases} 0 & \text{if } K^* < K_{\mathrm{IC}} \\ C_{\mathrm{R}}\left(1 - \frac{K_{\mathrm{IC}}}{K^*}\right) & \text{otherwise} \end{cases} \tag{60}$$

Then a crack increment will be $\triangle l = C \triangle t$, where $\triangle t$ is the timestep in the explicit algorithm. However, compared with the mesh size, this increment $\triangle l$ is too small to be recognized in the numerical simulation. A length related to the mesh size (generally half to one of the grid size) is taken as the crack growth increment to ensure the continuity of crack surface.

4.3.2 | The evolution of the crack surface

In 3D problem, the crack front is a spatial curve which consist of a group of line segments. As shown in Fig.9, the XMPM evaluates the stress intensity factors along the crack front (red segments) while modelling the crack propagation. Based on the dynamic crack propagation law described in section 4.3.1, the length and direction of the crack growth increment can be determined at each points. Then the next front points can be set (cyan points) in Fig.9(b). Connecting the current and next front points can obtain the newly crack surface, which is also discretized into the triangular elements (Fig.9(c)).

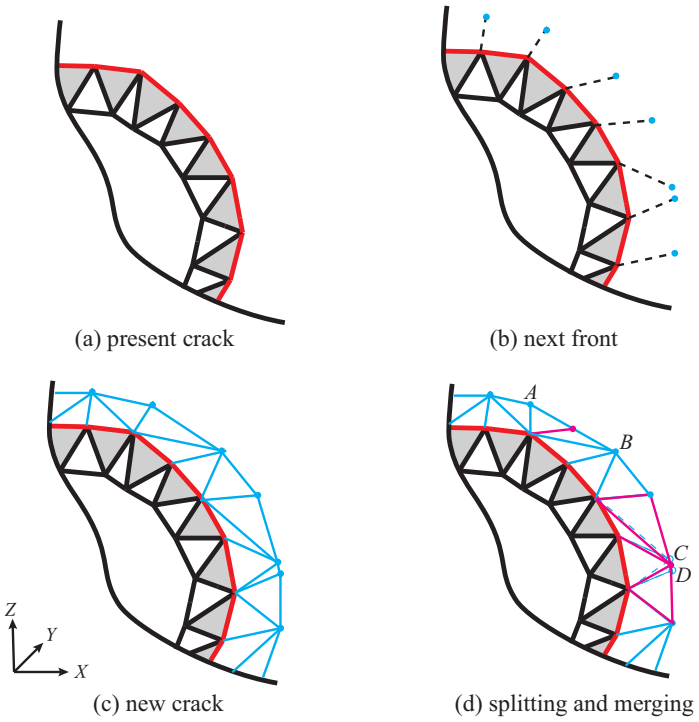

FIGURE 9 The update of crack fronts

During the simulation, the length of the crack front becomes shorter or longer. As shown in Fig.9(d), the line AB will be too long to effectively represent the crack surface, which means that it can't identify all the cells the crack passes through, while the line CD is so short that it's very sensitive to direction, which is used to build the local coordinate system for calculating the stress intensity factors. The XMPM will adaptively divide a longer line by two segments and merge the two endpoints of a shorter line. These techniques make the XMPM more stable while crack propagating.

The XMPM describes the crack surface independently of the background grid, which makes it possible to simulate the discontinuities in the elements. However, the crack front can extend beyond the boundary of the material domain. As shown in Fig.10, the hollow points represent the front points outside the material domain while the solid points inside the material domain. If the hollow points continue to expand, it will grow in an unpredictable direction. Therefore, after each crack propagation, those front lines completely outside the material domain, connected by two hollow points, will be marked and won't propagate again. Besides, if one hollow point goes inside the material domain, it will turns into a solid point and another hollow point will be set outside the material domain.

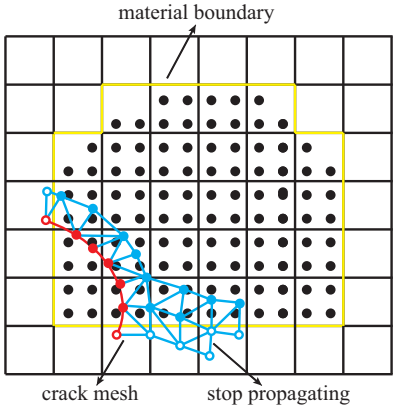

FIGURE 10 The crack front out of the material domain

5 | NUMERICAL EXAMPLES

The proposed XMPM has been implemented in our MPM3D code[38,53], and several numerical examples are studied in this section to verify and validate the method.

5.1 | The validation on capacity and efficiency of the XMPM

First, the capacity of XMPM to simulate crack problems including multiple cracks is studied. As shown in Fig.11, the specimens involve different numbers of cracks, that is 1, 2 and 4. This is a 2D problem but simulated in 3D procedure and the crack penetrates the plate in the direction of thickness. The plate has a size of 400mm × 120mm × 10mm and the mid-line of the cracks are located in the mid-plane of the plate and the angle between the crack surface relative to the mid-plane is defined as $\tan\theta = 2$. All the cracks are parallel and the horizontal distances are 200mm and 100mm for the two and four cracks cases respectively. The material has a density of $\rho = 1.5\text{g/cm}^3$, Young modulus of $E = 0.1$MPa and Poisson ratio of $\nu = 0.33$.

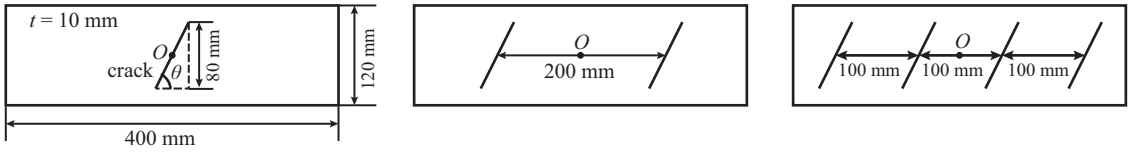

(a) 1 crack (b) 2 cracks (c) 4 cracks

FIGURE 11 The plates with different number of cracks

As mentioned before, the XMPM only needs to locally enrich the nodes around the crack surface so that the LSM values of the particles far away from the cracks are unnecessary, which enables the XMPM to simulate multiple uncrossed cracks without other techniques. Fig.12 shows the LSM values of particles need to be initialized for each crack.

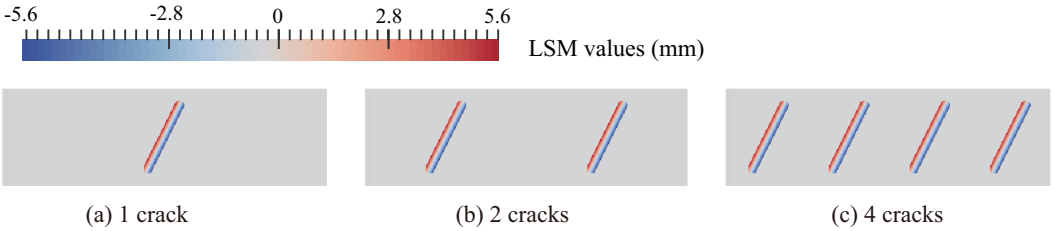

FIGURE 12 Level set function values around the cracks

A short-time axis impact load $\sigma = 100$MPa is applied on both sides of the plate. The distribution of the horizontal displacement, velocity and stress at $t = 25$ms are shown in Fig.13. They all show the discontinuities on both sides of the cracks and the stress field describes reasonable behaviours with concentrating stress around the crack tip.

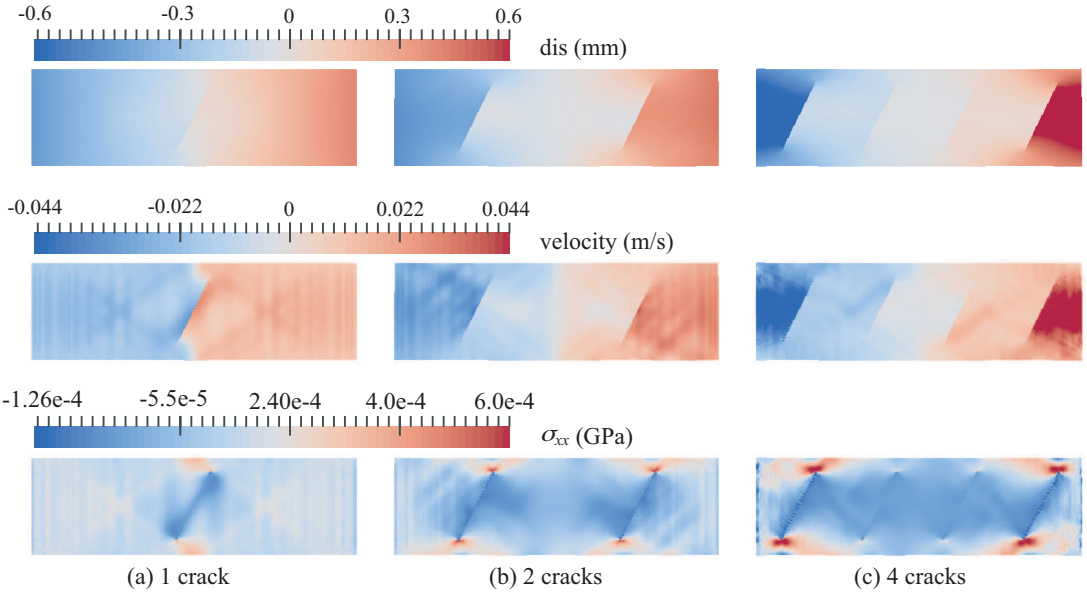

FIGURE 13 The horizontal distribution of the displacement, velocity and stress

Besides, the extra computational effort of the XMPM is also investigated based on this example. The relative extra cost of the XMPM is defined by

$$t_{\mathrm{r}} = \frac{t_{\mathrm{XMPM}} - t_{\mathrm{MPM}}}{t_{\mathrm{MPM}}} \tag{61}$$

All the simulations in this paper are run in a PC with one Intel(R) core(TM) i7-4790 CPU @ 3.60GHz. Table 1 compares the computational time used by the conventional MPM and XMPM, where the conventional MPM simulates the same problem without the cracks involved. The XMPM costs 14.01% more than the MPM to simulate a predefined crack, while it increases approximately to 18% for two cracks and 24% for four cracks respectively. It shows that the extra cost increases linearly with the number of cracks, which makes XMPM a potential way to simulate lots of cracks.

TABLE 1 Comparison in efficiency for different number of cracks

crack number	1	2	4
t_{MPM} (s)		82.372	
t_{XMPM} (s)	93.909	97.420	102.36
$t_{\mathrm{r}}(\%)$	14.01	18.27	24.27

5.2 | The static and dynamic stress intensity factor

In this section, the calculation of 3D stress intensity factors for both static and dynamic conditions is performed, which is introduced in Section 4 under the assumption of linear elasticity.

5.2.1 | A cylindrical bar with an inclined crack

First consider a cylindrical bar with an inclined circular crack shown in Fig. 14, which is also studied by CRAMP[80]. The cylindrical bar has a radius of $r = 50$mm and length of $l = 90$mm, where the crack has a radius of $a = 50$mm and the angle relative to the loading direction is $\phi = 60°$. The material has a density of $\rho = 7900\mathrm{kg/m^3}$, Young modulus of $E = 20$GPa and Poisson ratio of $\nu = 0.298$. The simulation uses a grid size of 1mm × 1mm × 1mm with initially two particles in each direction in each cell, and the radius of J-integral path is 4mm, four times the cell size.

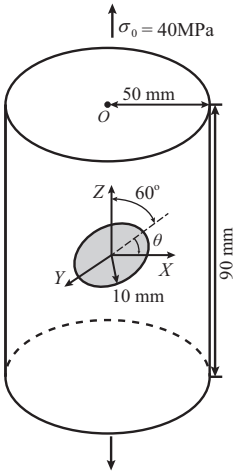

FIGURE 14 A cylindrical bar with an inclined crack

The specimen is subjected to a linear increasing load $\sigma(t)$ defined by Eq.(62) , to obtain the static solution for comparison with the analytical solution.

$$\sigma(t) = \begin{cases} \frac{t}{t_0}\sigma_0 & t < t_0 \\ \sigma_0 & t \geqslant t_0 \end{cases} \tag{62}$$

where $\sigma_0 = 40$MPa and the linear loading time t_0 is set to 0.75ms. Meanwhile the velocity damping is also applied. The simulation is continued to time $t = 1$s, when the velocity of the bar has approximately reached zero.

The analytical solution of stress intensity factors is given[81] as

$$K_{\mathrm{Ia}} = \frac{2}{\pi}\sigma\sqrt{\pi a}\cos^2\alpha \tag{63}$$

$$K_{\mathrm{IIa}} = \frac{4}{\pi(2-\nu)}\sigma\sqrt{\pi a}\cos\alpha\sin\alpha\cos\theta \tag{64}$$

$$K_{\mathrm{IIIa}} = \frac{4(1-\nu)}{\pi(2-\nu)}\sigma\sqrt{\pi a}\cos\alpha\sin\alpha\sin\theta \tag{65}$$

where $\alpha = 90° - \phi$ and θ is defined in Fig.14.

The distribution of all three stress intensity factors along the crack front are plotted in Fig.15, which are normalized by $K_0 = \frac{2}{\pi}\sigma\sqrt{\pi a}$. The simulation results agree well with the theoretical solutions. However, there exist differences where the XMPM has a bigger value. In XMPM, the elements are discontinuous as long as the crack enters them, which leads to a bigger crack dimension in XMPM simulation than the actual one, i.e. a. Therefore, the XMPM gets these results.

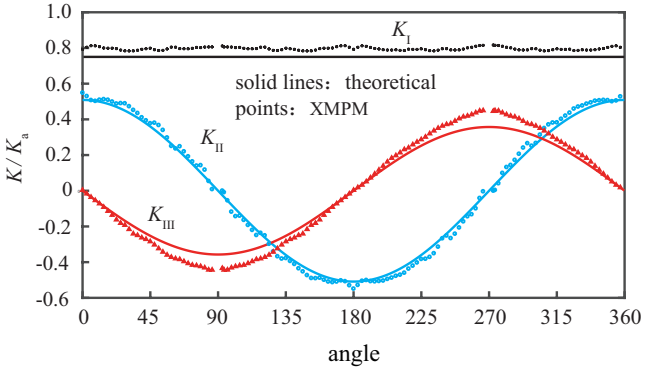

FIGURE 15 The static stress intensity factors along the crack front

5.2.2 | A rectangular specimen with an elliptical crack

Next, the dynamic stress intensity factor is studied. As shown in Fig.16, an elliptical crack is embedded in the mid-plane of a rectangular rod, which is subjected to an axial tensile load of $\sigma(t) = 400$MPa. The specimen has a size of 300mm × 180mm × 120mm and the axis of the elliptical crack are 70mm and 40mm respectively. Fig.16 shows only half of the specimen. The material has a density of $\rho = 7900\text{kg/m}^3$, Young modulus of $E = 200$GPa and Poisson ratio of $\nu = 0.298$. The simulation uses a grid size of 5mm × 5mm × 5mm with initially two particles at each direction in each cell, and the radius of J-integral path is 20mm, also four times the cell size.

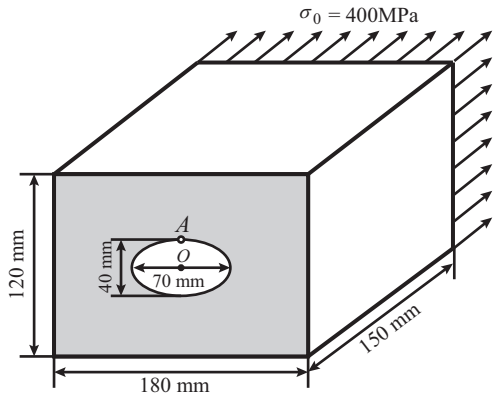

FIGURE 16 A rectangular specimen with an elliptical crack

The stress intensity factor of the point A in Fig.16 is calculated and the result is plotted in Fig.17. Other numerical methods including CRAMP[80], FEM[82] and FDM[83] also study this dynamic problem. The XMPM is more consistent with the CRAMP and FEM.

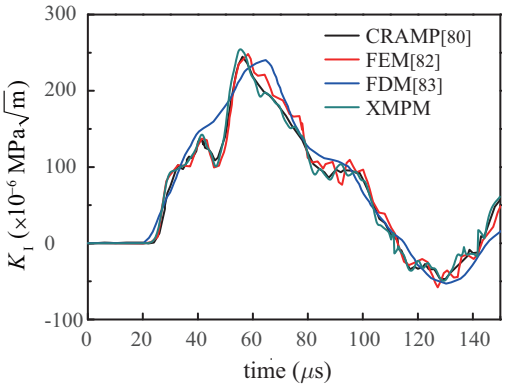

FIGURE 17 A cylindrical bar with an inclined crack

5.3 | The dynamic crack propagation

There are few studies on simulation of 3D crack propagation in the MPM framework. The section shows several examples[64] to demonstrate the capability of XMPM to handle the 3D crack propagation.

5.3.1 | The three-point bending with crack propagation

As shown in Fig.18, a three-point bending specimen with an edge crack, subjected to central impact, is modeled first. The specimen has a length of 400mm, a width of 100mm and a thickness of 10mm. The crack has an initial length of 50mm. This problem was experimentally studied by Nishioka[84]. The specimen has a density of $\rho = 1190\text{kg/m}^3$, Young modulus of $E = 2.94\text{GPa}$, Poisson ratio of $\nu = 0.3$, fracture toughness of $K_{\text{IC}} = 1.2\text{MPa}\sqrt{\text{m}}$ and is impacted by a cylindrical body, which has a mass of $m = 5.05\text{kg}$ and an initial velocity of $v_0 = 5\text{m/s}$. The stiff body is modeled with $E_c = 100\text{GPa}$ and $\nu_c = 0.25$.

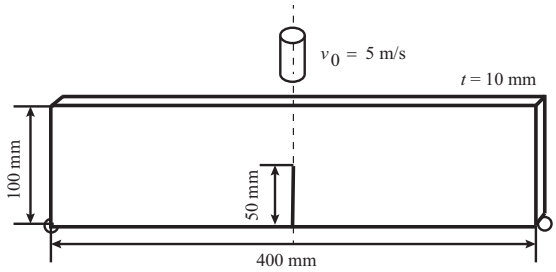

FIGURE 18 A three-point bending specimen with an edge crack

Due to the symmetry of the problem, the crack will grow along its initial crack plane as the SIF exceeds the fracture toughness. Fig.19 gives the crack length versus time obtained by the CRAMP, experiment and XMPM with different crack incremental length for each propagation. The results show that the XMPM accurately captures the crack first propagation time, which is approximately at $t = 0.16\text{ms}$. For the crack incremental length of 0.25 times element size, the propagation length agrees well with the experimental results.

The mixed mode crack is studied by moving the cylindrical body 20mm to the left as shown in Fig.20. This will lead to a change in the crack direction towards the impact point. The Fig.21 shows the evolution of the crack surface and the discontinuous displacement filed as expected. With the different grid size, 4mm, 2mm and 1mm, the crack propagation paths have a difference as shown in Fig.22, although the general direction is the same. However, the simulation results have a better agreement with the experimental results by refining the mesh.

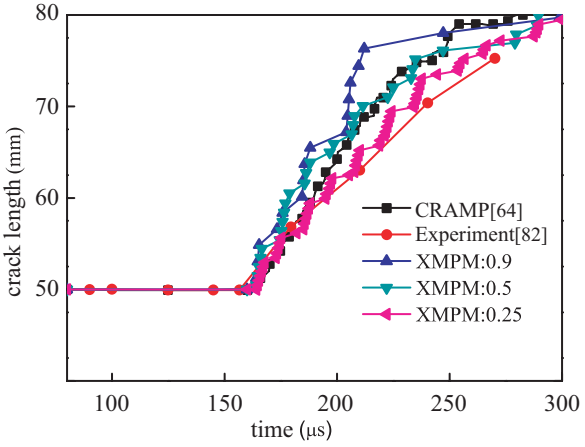

FIGURE 19 Crack length versus time with different crack incremental length

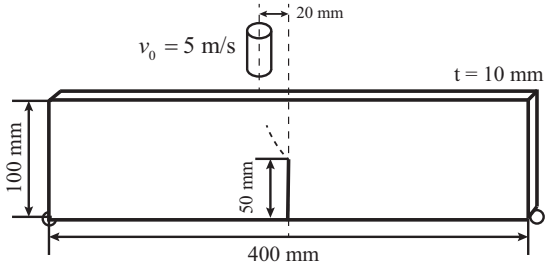

FIGURE 20 A three-point bending specimen subjected to the eccentric impact

5.3.2 | A square rod with an inclined crack

Consider a square rod with an quarter inclined crack located at the middle of one edge, as shown in Fig.23. The specimen has a size of 50mm × 50mm × 100mm and is subjected to an axis load of $\sigma = 100$MPa. The crack has a radius of 18.475mm and the angle relative to the edge is 60°. The material has a density of $\rho = 7900\text{kg/m}^3$, Young modulus of $E = 200$GPa, Poisson ratio of $\nu = 0.298$ and fracture toughness of $K_{\text{IC}} = 20\text{MPa}\sqrt{\text{m}}$.

Fig.24 shows evolutionary process of the crack patterns, including the crack surface mesh, LSM values of particles and the displacement nephogram. The crack pattern changes to mode I dominated type from mixed-mode after it starts to grow. With the propagation, the crack front gets longer and reaches to the rod boundary. Then it stops growing, which is seen at $t = 22.5$μs. Finally, the crack fully penetrates the specimen, two parts of which move separately. It shows the techniques in XMPM to handle the cracks propagation work well.

5.3.3 | A hollow tube with an inclined crack

A hollow tube with an inclined crack is then studied in this section. As shown in Fig.25, the tube has a length of $l = 100$mm, internal radius of $r = 35$mm and thickness of $t = 10$mm. The through-wall crack is centrally located at the mid-plane with a length of 14.14mm. The angle of the crack surface relative to the axis direction is 45°. The material used is the same as that in section 5.3.2, which has a density of $\rho = 7900\text{kg/m}^3$, Young modulus of $E = 200$GPa, Poisson ratio of $\nu = 0.298$ and fracture toughness of $K_{\text{IC}} = 20\text{MPa}\sqrt{\text{m}}$.

The evolution of the crack surface is shown in Fig.26. The similar conclusion is observed that the crack pattern changes to mode I dominated type from mixed-mode after it starts to grow for both crack fronts. This example also demonstrates the capability of the XMPM to handle the situation that the crack front interacts with materials boundaries while propagating.

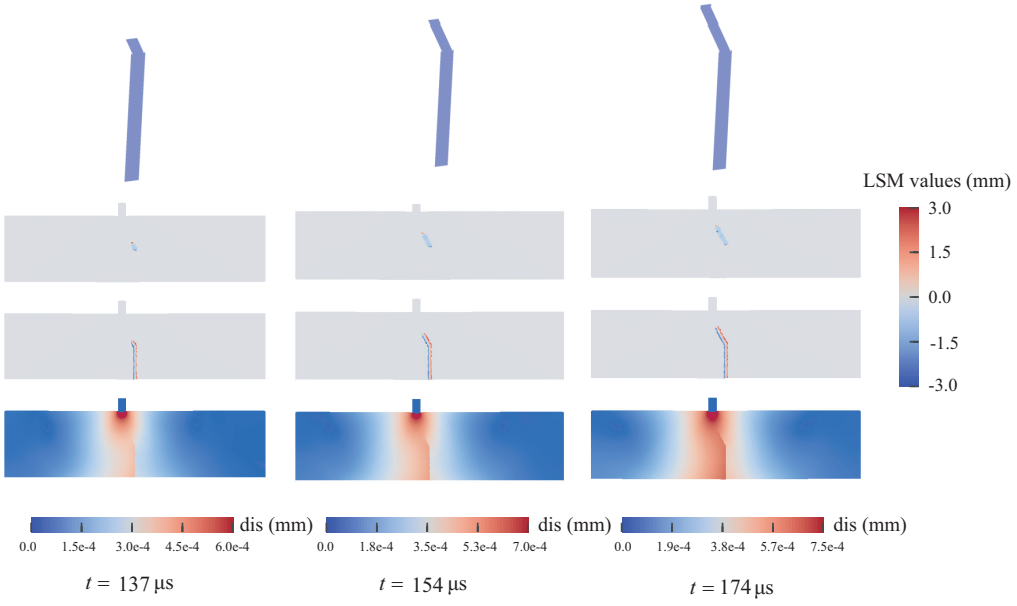

FIGURE 21 The evolution of the crack surface

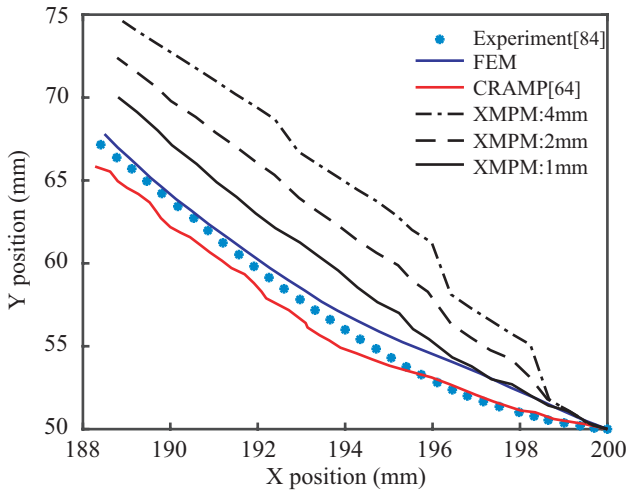

FIGURE 22 Crack propagation paths of three-point bending with eccentric impact

6 | CONCLUSION

In this paper, the XMPM is proposed for modelling 3D crack problems by introducing the idea of the XFEM into the MPM framework. The traditional MPM encounters difficulties in simulating discontinuities due to the continuous nodal shape function. The proposed XMPM enriches the nodal degrees of freedom in the region around the crack and employs jump function to describe the discontinuity on both sides of the crack. The discretization scheme of the XMPM is then derived from the weak form of the momentum conservation equations based on the modified particle displacement approximation, just as the conventional MPM. The XMPM introduces the discontinuity of the crack independent of the background grid with an extra set of crack surface mesh and the LSM is also employed to determine the nodal enriched function conveniently. It should be noted that only the particles near the crack need to be initialized to obtain the LSM values so that multiple uncrossed cracks can be handled directly by the XMPM. The efficiency study also shows the extra cost due to the existing cracks increases linearly with the number of cracks, in the form of increasing the number of the enriched nodes, which makes XMPM a potential way to simulate lots of cracks. The calculation of stress intensity factors for both static and dynamic conditions is performed to demonstrate the

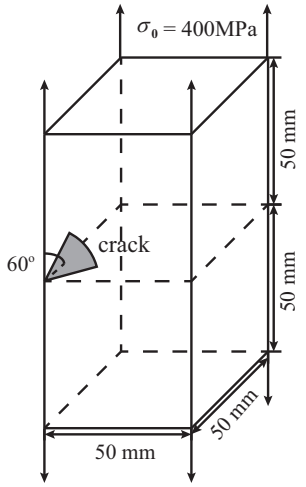

FIGURE 23 A square rod with an inclined crack

capability of XMPM to obtain the correct fracture parameters from the stress field, which also verified the results of simulation. To ensure the continuity and smoothness of the crack surface, a series of adaptive crack front processing methods is developed in the XMPM based on the crack surface mesh. The numerical examples show the cracks propagate as expected from mix-mode type to mode I dominated type and the techniques works well. However, the simulation of 3D crack propagation is still an area worthy of further study.

Data Availability Statement

The data that support the findings of this study are available from the corresponding author upon reasonable request.

References

1. Shank M. Brittle failure of steel structures-a brief history. *Metal Progress* 1954; 66(3): 83–83.
2. Griffith AA. VI. The phenomena of rupture and flow in solids. *Philosophical transactions of the royal society of london. Series A, containing papers of a mathematical or physical character* 1921; 221(582-593): 163–198.
3. Irwin GR. Analysis of stresses and strains near the end of a crack traversing a plate. *J. appl. Mech.* 1957; 24: 351–369.
4. Paris PC. A rational analytic theory of fatigue. *The trend in engineering* 1961; 13: 9–14.
5. Rice JR. A path independent integral and the approximate analysis of strain concentration by notches and cracks. *Journal of Applied Mechanics* 1968; 35(2): 379–386.
6. Cherepanov G. The propagation of cracks in a continuous medium. *Journal of Applied Mathematics and Mechanics* 1967; 31(3): 503–512.
7. Rice J, Rosengren GF. Plane strain deformation near a crack tip in a power-law hardening material. *Journal of the Mechanics and Physics of Solids* 1968; 16(1): 1–12.
8. Miehe C, Gürses E. A robust algorithm for configurational-force-driven brittle crack propagation with R-adaptive mesh alignment. *International Journal for Numerical Methods in Engineering* 2007; 72(2): 127–155.
9. Xu XP, Needleman A. Numerical simulations of fast crack growth in brittle solids. *Journal of the Mechanics and Physics of Solids* 1994; 42(9): 1397–1434.

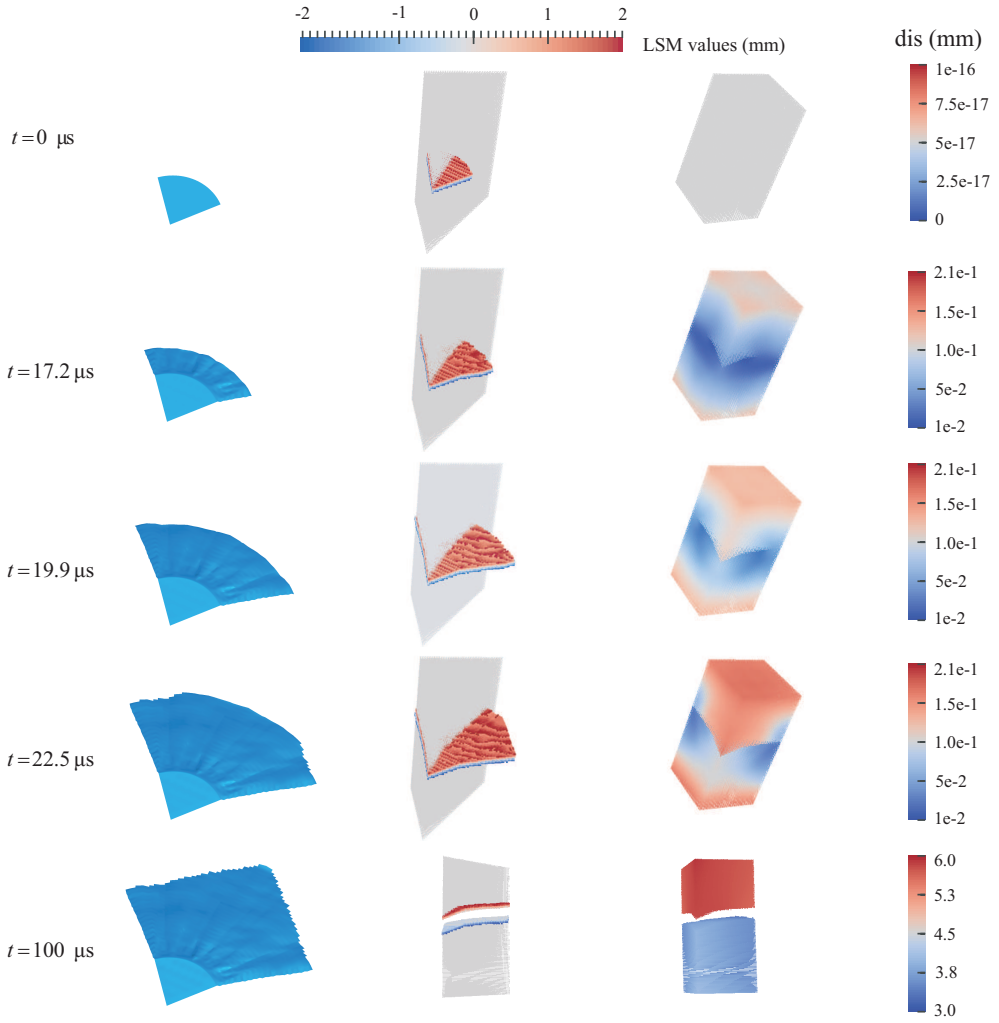

FIGURE 24 The evolution of the crack patterns

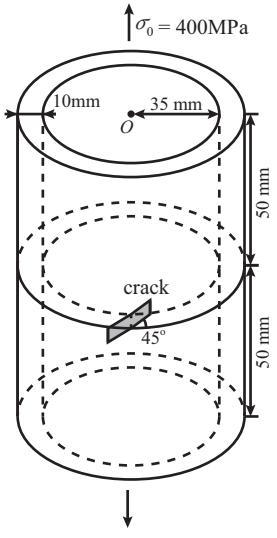

FIGURE 25 A square rod with an inclined crack

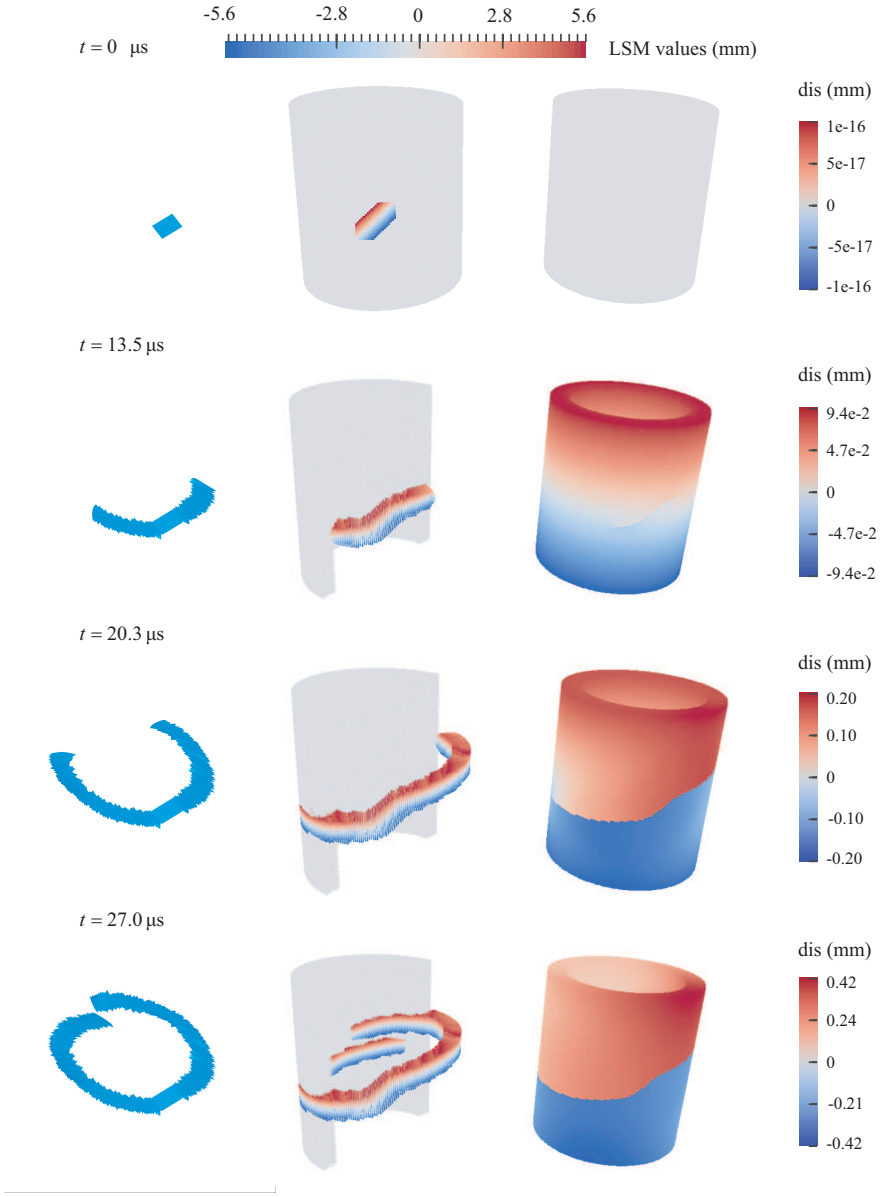

FIGURE 26 The evolution of the crack surface

10. Belytschko T, Fish J, Engelmann BE. A finite element with embedded localization zones. *Computer Methods in Applied Mechanics and Engineering* 1988; 70(1): 59–89.

11. Belytschko T, Black T. Elastic crack growth in finite elements with minimal remeshing. *International journal for numerical methods in engineering* 1999; 45(5): 601–620.

12. Moës N, Dolbow J, Belytschko T. A finite element method for crack growth without remeshing. *International Journal for Numerical Methods in Engineering* 1999; 46(1): 131–150.

13. Melenk JM, Babuska I. The partition of unity finite element methods: Basic theory and applications. *Computer Methods in Applied Mechanics and Engineering* 1996; 139(1-4): 289-314.

14. Babuska I, Melenk JM. The partition of unity finite element method. *International Journal for Numerical Methods in Engineering* 1997; 40(4): 727-758.

15. Sukumar N, Huang Z, Prévost JH, Suo Z. Partition of unity enrichment for bimaterial interface cracks. *International journal for numerical methods in engineering* 2004; 59(8): 1075–1102.

16. Asadpoure A, Mohammadi S. Developing new enrichment functions for crack simulation in orthotropic media by the extended finite element method. *International Journal for Numerical Methods in Engineering* 2007; 69(10): 2150–2172.

17. Rojas-Díaz R, Sukumar N, Sáez A, García-Sánchez F. Fracture in magnetoelectroelastic materials using the extended finite element method. *International Journal for Numerical Methods in Engineering* 2011; 88(12): 1238–1259.

18. Yu T, Shi L. Determination of sharp V-notch stress intensity factors using the extended finite element method. *The Journal of Strain Analysis for Engineering Design* 2012; 47(2): 95–103.

19. Moës N, Belytschko T. Extended finite element method for cohesive crack growth. *Engineering fracture mechanics* 2002; 69(7): 813–833.

20. Unger JF, Eckardt S, Könke C. Modelling of cohesive crack growth in concrete structures with the extended finite element method. *Computer methods in applied mechanics and engineering* 2007; 196(41-44): 4087–4100.

21. Belytschko T, Moës N, Usui S, Parimi C. Arbitrary discontinuities in finite elements. *International Journal for Numerical Methods in Engineering* 2001; 50(4): 993–1013.

22. Daux C, Moës N, Dolbow J, Sukumar N, Belytschko T. Arbitrary branched and intersecting cracks with the extended finite element method. *International journal for numerical methods in engineering* 2000; 48(12): 1741–1760.

23. Budyn E, Zi G, Moës N, Belytschko T. A method for multiple crack growth in brittle materials without remeshing. *International Journal for Numerical Methods in Engineering* 2004; 61(10): 1741–1770.

24. Taleghani AD. *Analysis of hydraulic fracture propagation in fractured reservoirs: An improved model for the interaction between induced and natural fractures*. PhD thesis. The University of Texas at Austin, 2009.

25. Belytschko T, Lu YY, Gu L. Element free Galerkin methods. *International Journal for Numerical Methods in Engineering* 1994; 37: 229-256.

26. Lu Y, Belytschko T, Gu L. A new implementation of the element free Galerkin method. *Computer methods in applied mechanics and engineering* 1994; 113(3-4): 397–414.

27. Belytschko T, Krongauz Y, Organ D, Fleming M, Krysl P. Meshless methods: An overview and recent developments. *Computer Methods in Applied Mechanics and Engineering* 1996; 139(1-4): 3–47.

28. Belytschko T, Lu Y, Gu L. Crack propagation by element-free Galerkin methods. *Engineering Fracture Mechanics* 1995; 51(2): 295–315.

29. Lu Y, Belytschko T, Tabbara M. Element-free Galerkin method for wave propagation and dynamic fracture. *Computer Methods in Applied Mechanics and Engineering* 1995; 126(1-2): 131–153.

30. Belytschko T, Lu Y, Gu L, Tabbara M. Element-free Galerkin methods for static and dynamic fracture. *International Journal of Solids and Structures* 1995; 32(17-18): 2547–2570.

31. Fleming M, Chu Y, Moran B, Belytschko T. Enriched element-free Galerkin methods for crack tip fields. *International journal for numerical methods in engineering* 1997; 40(8): 1483–1504.

32. Rao B, Rahman S. An efficient meshless method for fracture analysis of cracks. *Computational mechanics* 2000; 26(4): 398–408.

33. Rao B, Rahman S. Mesh-free analysis of cracks in isotropic functionally graded materials. *Engineering fracture mechanics* 2003; 70(1): 1–27.

34. Liu WK, Hao S, Belytschko T, Li S, Chang CT. Multiple scale meshfree methods for damage fracture and localization. *Computational materials science* 1999; 16(1-4): 197–205.

35. Dolbow J, Moës N, Belytschko T. Discontinuous enrichment in finite elements with a partition of unity method. *Finite elements in analysis and design* 2000; 36(3-4): 235–260.

36. Shedbale A, Singh I, Mishra B, Sharma K. Ductile failure modeling and simulations using coupled FE-EFG approach. *International Journal of Fracture* 2017; 203(1-2): 183–209.

37. Sulsky D, Chen Z, Schreyer HL. A Particle Method for History-Dependent Materials. *Computational Methods Applied in Mechanical Engineering* 1994; 118: 179-186.

38. Zhang X, Chen Z, Liu Y. *The Material Point Method: A Continuum-Based Particle Method for Extreme Loading Cases*. Academic Press . 2016.

39. Bardenhagen SG, Kober EM. The Generalized Interpolation Material Point Method. *CMES-Computer Modeling in Engineering & Sciences* 2004; 5(6): 477-495.

40. Wallstedt PC, Guilkey J. An evaluation of explicit time integration schemes for use with the generalized interpolation material point method. *Journal of Computational Physics* 2008; 227(22): 9628–9642.

41. Ma S. *Material point meshfree methods for impact and explosion problems*. PhD thesis. Tsinghua University Beijing, 2009.

42. Charlton T, Coombs W, Augarde C. iGIMP: an implicit generalised interpolation material point method for large deformations. *Computers & Structures* 2017; 190: 108–125.

43. Sadeghirad A, Brannon RM, Burghardt J. A convected particle domain interpolation technique to extend applicability of the material point method for problems involving massive deformations. *International Journal for Numerical Methods in Engineering* 2011; 86(12): 1435–1456.

44. Zhang DZ, Ma X, Giguere PT. Material point method enhanced by modified gradient of shape function. *Journal of Computational Physics* 2011; 230(16): 6379–6398.

45. Steffen M, Wallstedt PC, Guilkey JE, Kirby RM, Berzins M. Examination and analysis of implementation choices within the Material Point Method (MPM). *CMES-Computer Modeling in Engineering & Sciences* 2008; 31(2): 107-127.

46. Gong M. *Improving the material point method*. PhD thesis. University of New Mexico, 2015.

47. Liang Y, Zhang X, Liu Y. An efficient staggered grid material point method. *Computer Methods in Applied Mechanics and Engineering* 2019; 352: 85–109.

48. Liu Y, Wang HK, Zhang X. A multiscale framework for high-velocity impact process with combined material point method and molecular dynamics. *International Journal of Mechanics and Materials in Design* 2013; 9(2): 127–139.

49. Huang P, Zhang X, Ma S, Wang H. Shared memory OpenMP parallelization of explicit MPM and its application to hypervelocity impact. *CMES-Computer Modeling in Engineering & Sciences* 2008; 38(2): 119–148.

50. Hu W, Chen Z. Model-based simulation of the synergistic effects of blast and fragmentation on a concrete wall using the MPM. *International Journal of Impact Engineering* 2006; 32(12): 2066–2096.

51. Ma S, Zhang X, Lian Y, Zhou X. Simulation of high explosive explosion using adaptive material point method. *CMES-Computer Modeling in Engineering & Sciences* 2009; 39(2): 101.

52. Wang Y, Beom H, Sun M, Lin S. Numerical simulation of explosive welding using the material point method. *International Journal of Impact Engineering* 2011; 38(1): 51–60.

53. Ma Z, Zhang X, Huang P. An object-oriented MPM framework for simulation of large deformation and contact of numerous grains. *CMES-Computer Modeling in Engineering & Sciences* 2010; 55(1): 61.

54. Gong W, Zhang X, Qiu X. Numerical study of dynamic compression process of aluminum foam with material point method. *CMES-Computer Modeling in Engineering & Sciences* 2011; 82(3-4): 195–213.

55. Yang P, Liu Y, Zhang X, Zhou X, Zhao Y. Simulation of fragmentation with material point method based on Gurson model and random failure. *CMES-Computer Modeling in Engineering & Sciences* 2012; 85(3): 207–237.

56. Shen LM. A Rate-Dependent Damage/Decohesion Model for Simulating Glass Fragmentation under Impact using the Material Point Method. *CMES-Computer Modeling in Engineering & Sciences* 2009; 49(1): 23–45.

57. Zhang DZ, Zou Q, VanderHeyden WB, Ma X. Material point method applied to multiphase flows. *Journal of Computational Physics* 2008; 227(6): 3159–3173.

58. Liang D, Zhao X, Martinelli M. MPM Simulations of the Interaction Between Water Jet and Soil Bed. *Procedia Engineering* 2017; 175: 242–249.

59. Rohe A, Liang D. Modelling large deformation and soil-water-structure interaction with material point method: Briefing on MPM2017 conference. *Journal of Hydrodynamics* 2017; 29(3): 393–396.

60. Lian YP, Zhang X, Liu Y. Coupling of finite element method with material point method by local multi-mesh contact method. *Computer Methods in Applied Mechanics and Engineering* 2011; 200: 3482-3494.

61. Nairn JA. Material Point Method Calculations with Explicit Cracks. *CMES-Computer Modeling in Engineering & Sciences* 2003; 4(6): 649-663.

62. Guo YJ, Nairn JA. Calculation of J-Integral and Stress Intensity Factors using the Material Point Method. *CMES-Computer Modeling in Engineering & Sciences* 2004; 6(3): 295-308.

63. Guo Y, Nairn J. Three-dimensional dynamic fracture analysis using the material point method. *Computer Modeling in Engineering and Sciences* 2006; 16(3): 141.

64. Guo Y, Nairn J. Simulation of dynamic 3D crack propagation within the material point method. *Computer Modeling in Engineering & Sciences* 2017; 113(4): 389–410.

65. Liang Y, Benedek T, Zhang X, Liu Y. Material point method with enriched shape function for crack problems. *Computer Methods in Applied Mechanics and Engineering* 2017; 322: 541–562.

66. Kakouris E, Triantafyllou SP. Phase-field material point method for brittle fracture. *International Journal for Numerical Methods in Engineering* 2017; 112(12): 1750–1776.

67. Kakouris E, Triantafyllou SP. Phase-Field Material Point Method for dynamic brittle fracture with isotropic and anisotropic surface energy. *Computer Methods in Applied Mechanics and Engineering* 2019; 357: 112503.

68. Cheon Y, Kim HG. An adaptive material point method coupled with a phase-field fracture model for brittle materials. *International Journal for Numerical Methods in Engineering* 2019; 120(8): 987–1010.

69. Soga K, Alonso E, Yerro A, Kumar K, Bandara S. Trends in large-deformation analysis of landslide mass movements with particular emphasis on the material point method. *Géotechnique* 2016; 66(3): 248–273.

70. Melenk JM, Babuska I. The partition of unity finite element method: Basic theory and applications. *Computer Methods in Applied Mechanics and Engineering* 1996; 139: 289–314.

71. Duarte CA, Oden JT. An h-p adaptive method using clouds. *Computer Methods in Applied Mechanics and Engineering* 1996; 139: 237–262.

72. Osher S, Sethian JA. Fronts propagating with curvature-dependent speed: algorithms based on Hamilton-Jacobi formulations. *Journal of computational physics* 1988; 79(1): 12–49.

73. Belytschko T, Stolarska M, Chopp DL, Moës N. Modelling crack growth by level sets in the extended finite element method. *International Journal for Numerical Methods in Engineering* 2001; 51: 943-960.

74. Nishioka T, Atluri S. Path-independent integrals, energy release rates, and general solutions of near-tip fields in mixed-mode dynamic fracture mechanics. *Engineering Fracture Mechanics* 1983; 18(1): 1–22.

75. Nishioka T, Stan F, Fujimoto T. Dynamic J Integral and Dynamic Stress Intensity Factor Distributions along Naturally and Dynamically Propagating Three-Dimensional Fracture Fronts. *Jsme International Journal Series A-solid Mechanics and Material Engineering* 2002; 45(4): 523–537.

76. Erdogan F, Sih G. On the crack extension in plates under plane loading and transverse shear. *Journal of Basic Engineering* 1963; 85(4): 519–527.

77. Freund L. Crack propagation in an elastic solid subjected to general loading – I. Constant rate of extension. *Journal of the Mechanics and Physics of Solids* 1972; 20(3): 129–140.

78. Grégoire D, Maigre H, Rethore J, Combescure A. Dynamic crack propagation under mixed-mode loading – comparison between experiments and X-FEM simulations. *International Journal of Solids and Structures* 2007; 44(20): 6517–6534.

79. Kanninen MF, Popelar CL. *Advanced Fracture Mechanics*. Oxford University Press . 1985.

80. Guo YJ, Nairn JA. Three-Dimensional Dynamic Fracture Analysis Using the Material Point Method. *CMES-Computer Modeling in Engineering & Sciences* 2006; 1(1): 11-25.

81. Tada H. The stress analysis of cracks handbook.; 2000.

82. Nishioka T. Recent developments in computational dynamic fracture mechanics. In: Computational Mechanics Publications. 1995.

83. Chen Y, Wilkins M. Numerical analysis of dynamic crack problems. *Mechanics of Fracture* 1977; 4: 295–345.

84. Nishioka T, Tokudome H, Kinoshita M. Dynamic fracture-path prediction in impact fracture phenomena using moving finite element method based on Delaunay automatic mesh generation. *International Journal of Solids and Structures* 2001; 38(30-31): 5273–5301.